J of Astronaut Sci (2015) 62:233–253
DOI 10.1007/s40295-015-0075-8

Touchless Electrostatic Three-dimensional Detumbling of Large Axi-symmetric Debris

Trevor Bennett[1] · **Hanspeter Schaub**[2]

Published online: 27 November 2015

Abstract Touchless detumbling of space debris is investigated to enable orbital servicing or active debris removal. Using active charge transfer between a servicer and debris object, control torques are created to reduce the debris spin rate prior to making any physical contact. In this work, the servicer shape is spherical and the debris is assumed to be cylindrical and tumbling. The attitude control goal is to reduce the debris tumbling motion while maintaining a fixed position ahead of the debris object. Prior work has identified the feasibility of electrostatic detumble for one degree of rotational freedom. This work extends the theory to three-dimensional tumbling motion. Using the previously developed Multi-Sphere modeling method for electrostatic forces and torques on non-spherical objects, detumble behavior is predicted and Lyapunov control theory and numerical simulations are used to demonstrate a stabilizing attitude control.

Keywords Electrostatic · GEO · Touchless detumble

Introduction

Electrostatic actuation has applications in orbital servicing, fractionated satellite concepts, formation flying applications such as telescope arrays, rendezvous and

✉ Trevor Bennett
Trevor.Bennett@Colorado.edu

[1] Graduate Research Assistant, Department of Aerospace Engineering Sciences, University of Colorado, 431 UCB, Colorado, Center for Astrodynamics Research, Boulder, CO 80309-0431, USA

[2] Alfred T. and Betty E. Look Professor of Engineering, Associate Chair of Graduate Affairs, Department of Aerospace Engineering Sciences, University of Colorado, 431 UCB, Colorado, Center for Astrodynamics Research, Boulder, CO 80309-0431, USA

docking control, and many other mission concepts that involve proximity operations. This study further develops general electrostatic relative attitude control exemplified by orbital space debris mitigation and servicing for bodies in Geosynchronous orbits. For example, defunct dual-spin spacecraft or spent upper-stage boosters form a significant part of the GEO debris population and help motivate this study. These objects of interest may tumble at rates of 10's of degrees per second [1], exceeding the servicing capabilities of current docking or grappling techniques [2]. Orbital servicing is a challenging space mission concept that requires an active host vehicle to approach, and mechanically interface with a defunct satellite or satellite component [3–5]. If the debris is tumbling, the process of docking onto the debris presents challenges and collision risks. Advanced docking systems, such as those being developed by MDA, discuss a maximum tumble rate of 1 degree/second for autonomous docking [2]. A touchless method of detumbling a passive object would greatly simplify the rendezvous and docking phase of an orbital servicer, and is the focus of this paper. Reference [6] discusses how electrostatic torque can be controlled to apply torques

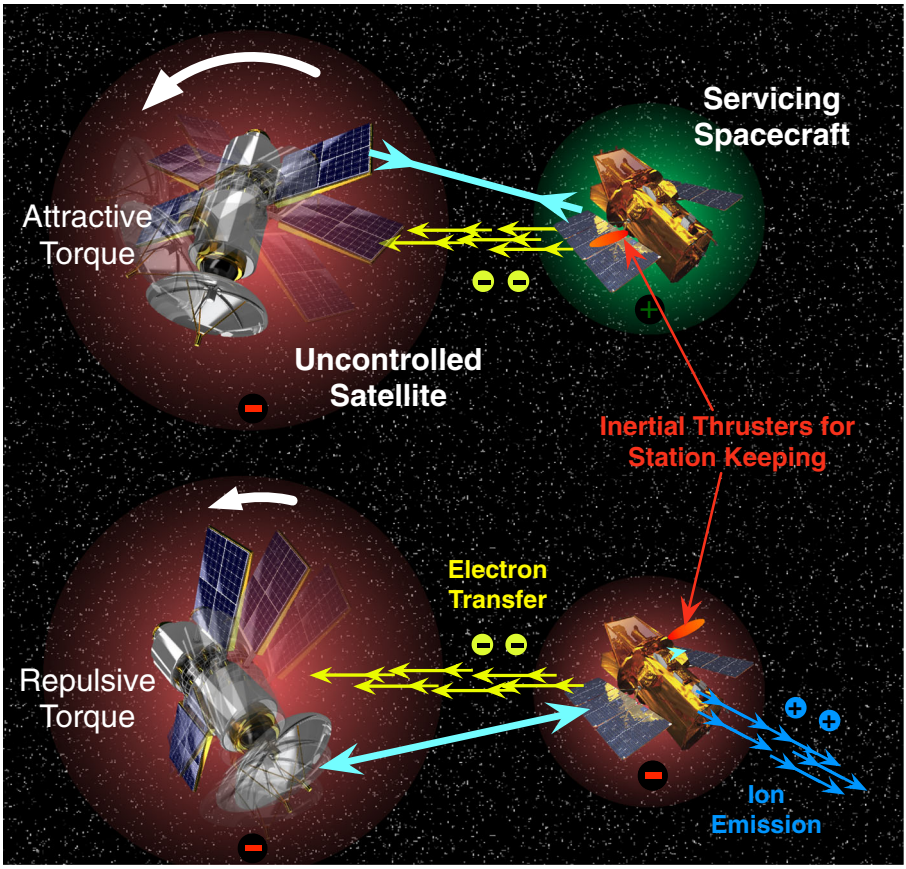

Fig. 1 Electrostatic actuation technology enabling diverse service mission profiles

on a spinning debris object without requiring physical contact as shown in Fig. 1. The charging is controlled through an electron or ion gun that charges the servicer positively or negatively and the debris positively. Such electrostatic actuation with a passive object is called an Electrostatic Tractor (ET), and is being considered for both large GEO debris mitigation [7–9] as well as touchless asteroid spin control [10, 11].

Electrostatic actuation of spacecraft has been explored since the 1960s. Reference [12] shows that the Geosynchronous Orbit environment is a candidate region where space plasma conditions enable Debye lengths on the order of 100's of meters with electrostatic control requiring only Watt-level power requirements. The feasibility of electrostatic control and actuation in space has been studied by several authors exploring both applications and charging dynamics [13–19]. The electrostatic forces exerted on the target body are possible because spacecraft are coated with outer conducting Mylar sheaths. The Mylar sheath is expected to remain intact and fixed to the target object because the forces exerted are on the order of milli-newtons. Reference [20] demonstrates that Mylar structures can sustain the voltage and forces exerted. Electrostatic detumble control could reduce the non-cooperative spacecraft rates prior to using other proximity or docking operations while minimizing onboard fuel usage.

The prospect of fuel efficiency in implementing electrostatic actuation is subject to a small increase in spacecraft complexity and highly-coupled nonlinear differential equations [21]. Electrostatic interaction between two spacecraft in a vacuum is accurately determined using finite element methods; however, these methods are computationally expensive and time intensive. Overcoming the modeling complexity enables onboard and autonomous spacecraft control through control of relative potentials on itself and another spacecraft or uncooperative body. Stevenson and Schaub introduce a new method called the Multi-Sphere Method (MSM) [21, 22] that approximates the electrostatic interaction between spacecraft with orders of magnitude less computational time than finite element methods, enabling faster-than-realtime attitude simulations and control developments. The multi-sphere method, summarized in the following sections, partitions the spacecraft volume into many electrostatically charged conducting spheres constrained by a spacecraft potential. Using the recently developed MSM technique, Reference [6] studies the charged relative one-dimensional rotational dynamics of a non-cooperative cylinder and a spherical charge-controlled spacecraft. A Lyapunov control development is provided to analytically guarantee global stability of the spin rate with the nominal ET force is assumed to be zero. The MSM result is used in numerical simulation to validate the expected control performance for all these 1-D despin scenarios. An experimental setup demonstrating electrostatic detumble control for 1-D cylinder rotation is discussed in Reference [23].

The focus of this study is the generalization of the one-dimensional cylinder detumble control to three-dimensional detumble control using Lyapunov control techniques and the MSM electrostatic force model. The study considers a non-cooperative tumbling cylinder and a spherical control spacecraft, or servicer, separated by a fixed distance, analogous to the GEO rocket body scenario. As in earlier studies, the objects are assumed to be in deep space, and additional perturbations are assumed to be negligible. Applying electrostatic detumble to a deep space case

decouples the orbital motion to study the effects of a 3-D detumble control law and to gain intuition about steady-state behavior. Future studies will apply the 3-D detumble control in the GEO regime where the Debye length is most favorable and the orbital motion influence can be studied. The focus of this work is to investigate how general three-dimensional rotation can be arrested with a servicer sphere at a fixed relative location. This work serves as a key step towards the development of modeling and control strategies of general 3-dimensional geometries that may include flexible appendages. Greater complexity may later be added by including flexible structures and residual propellent dynamics. The more complexity introduces resonance considerations. However, the tumble rates currently considered are less than 10°/sec with detumble dynamics often 2 orders of magnitude slower than resonant frequencies near 1 Hz leaving the interesting questions about on-rigid dynamics and resonance to future studies. Electrostatic detumble benefits in cases where energy dissipation from non-rigid body dynamics is present. Reference [6] postulates a simplified rigid body electrostatic torque model with separation of the voltage and attitude dependent components. This assumption is shown to be good if the separation distance is at least 3-4 craft radii. In this paper this separation of voltage and attitude dependency of the electrostatic torque is investigated in more detail for debris undergoing three-dimensional rotations. Of interest are how torque equilibria impact the convergence of the general tumbling scenario, the stability of such equilibria, and the development of a general detumble ET control algorithm. The following sections detail the Multi-Sphere Method, the torque development, and proposed control structure. The paper concludes with numerical simulations and analysis.

Overview of the Multi-Sphere Method

The Multi-Sphere Method (MSM) represents the complete spacecraft electrostatic charging model as a collection of spherical conductors dispersed through the body [21] to provide induced charging effects consistent with finite element methods. The cylinder configuration with a 3 sphere MSM, representative of the above mentioned rocket bodies and defunct spacecraft, is presented in Fig. 2. Visible are the electrostatic forces between spheres, the projection angle for the torque controller, and the inertial station keeping thrust.

The three-sphere MSM approximation provides sufficient force and torque accuracy, within a percent of the finite element solution, for the separation distances considered [22]. All three conducting spheres are centered along the long axis of the cylinder which provides a diagonal moment of inertia matrix and symmetric charging. These two simplifications are crucial in the analysis presented here. The MSM geometric parameters used in this analysis are shown in Table 1.

The cylinder in this study tumbles with three rotational degrees of freedom. Figure 2 presents the two-craft configuration with projection angle defined. The modeled control parameters are the separation distance d of the mass centers along the separation vector $\hat{\boldsymbol{r}}$ and the controlled potentials ϕ_1 and ϕ_2 corresponding to the servicing spacecraft and cylinder respectively. The non-rotating coordinate system

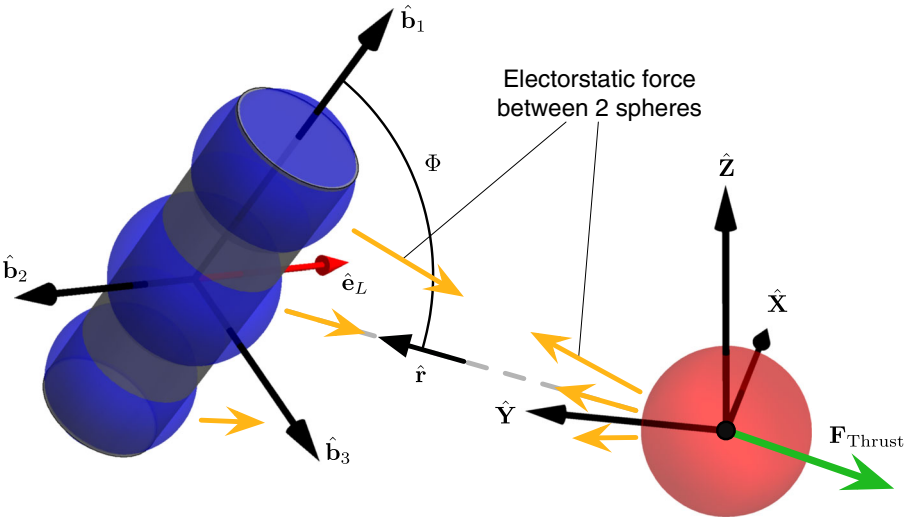

Fig. 2 3 sphere MSM cylinder and spherical spacecraft configuration

fixed to the servicer spacecraft and initially has the y-axis aligned with the separation vector $\hat{\boldsymbol{r}}$, the z axis pointed up, and the x axis completing a right-handed system. The cylinder has body fixed coordinates with $\hat{\boldsymbol{b}}_1$ through the long axis, and with $\hat{\boldsymbol{b}}_2$ and $\hat{\boldsymbol{b}}_3$ in the right handed transverse directions. The non-rotating and cylinder fixed frames are graphically represented in Fig. 2. Prior to exploring the projection angle shown in Fig. 2, the cylinder attitude is characterized by a rotation about the inertial z axis θ, and a pitch angle defined as a positive $\hat{\boldsymbol{b}}_2$ rotation. The rotation angle $\theta = 0$ and the pitch angle $\psi = 0$ when the cylinder $\hat{\boldsymbol{b}}_1$ axis is aligned with the vector from the commanding spacecraft mass center to the cylinder mass center.

The electrostatic forces are determined by the charges residing on each sphere. These result from the prescribed electric potentials, according to the self and mutual capacitance relationships in Eq. 1, where $k_c = 8.99 \times 10^9$ N·m^2/C^2 and q_i is the charge of each sphere [24, 25].

$$\phi_i = k_c \frac{q_i}{R_i} + \sum_{j=1, j\neq i}^{m} k_c \frac{q_j}{r_{i,j}} \tag{1}$$

Table 1 MSM parameters for cylinder detumble system

Parameter	Value	Units	Description
d	15	m	Object center-to-center separation
l	1.1569	m	Outer sphere offset
R_a, R_c	0.5909	m	Outer sphere radius
R_b	0.6512	m	Central sphere radius

where R_i denotes the radius of the i^{th} conducting sphere and $r_{i,j}$ denotes the vector between the i^{th} and j^{th} conducting spheres. These forces are shown emanating from each sphere in Fig. 2. These relations can be collected in matrix form

$$\begin{bmatrix} \phi_1 \\ \phi_2 \\ \vdots \\ \phi_2 \end{bmatrix} = k_c \begin{bmatrix} 1/R_1 & 1/r_a & 1/r_b & 1/r_c \\ 1/r_a & 1/R_{2,a} & 1/l & 1/2l \\ 1/r_b & 1/l & 1/R_{2,b} & 1/l \\ 1/r_c & 1/2l & 1/l & 1/R_{2,c} \end{bmatrix} \begin{bmatrix} q_1 \\ q_a \\ q_b \\ q_c \end{bmatrix} \tag{2}$$

Inverting the matrix multiplying the charge at a given instant in time produces the forces and torques on the cylinder given by the summations

$$\boldsymbol{F}_2 = k_c q_1 \sum_{i=a}^{c} \frac{q_i}{r_i^3} \boldsymbol{r}_i \tag{3a}$$

$$\boldsymbol{L}_2 = k_c q_1 \sum_{i=a}^{c} \frac{q_i}{r_i^3} \boldsymbol{r}_{2,i} \times \boldsymbol{r}_i \tag{3b}$$

The servicer and cylinder remain at a constant separation distance, requiring the servicer inertial thrusting to counter-balance the net attractive or repulsive electrostatic forces. The control developed here assumes the necessary thrust force is present such that the system is moving in space yet the relative distance remains fixed allowing the spacecraft to be considered stationary for the control development and analysis.

Analytic Electrostatic Torque Approximations

Equation 3b provides an analytic torque expression. However, the square matrix has a size equivalent to the number of MSM spheres and couples the control potential ϕ to the attitude information through the resultant sphere charges q_i. Therefore, the equilibrium states, stability of the system, and control development are more easily explored using an analytic approximation of the MSM torque.

One-Dimensional Rotation Review

As shown by Reference [6], if the separation distance is sufficiently large, the potential and attitude influence on the electrostatic torque can be separated as shown in Eq. 4 where θ represents a 1-D attitude rotation measure.

$$L = \gamma f(\phi)\, g(\theta) \tag{4}$$

where L is the torque magnitude and γ is a model calibration constant. The separation of the potential dependence function $f(\phi)$ and the orientation dependence function $g(\theta)$ allows for a simplified analytic study in-place of the matrix form in Eq. 2. Without loss of generality, the non-cooperative cylinder is assumed to have the same

potential magnitude as the servicer, that is $\phi_2 = |\phi_1|$, and is assumed to be always positive [6]. Thus, the voltage dependency function is set to [6]:

$$f(\phi) = \phi|\phi| \tag{5}$$

The orientation angle dependency explored by Reference [6] presents (6) as the analytic representation. Reference [6] also demonstrates more complicated torque surfaces character at close proximity not captured due to induced charging properties. Using the simulation states shown in Table 1, the function

$$g(\theta) = \sin(2\theta) \tag{6}$$

provides a good approximation of the MSM developed torque surface with a correlation of $R^2 = 0.998$ and the tuned scaling parameter $\gamma = 2.234 \times 10^{-14}$ [6]. Using the potential and orientation dependency functions in Eq. 4 provides a separable form base function to approximate the MSM torque profile. Setting $\theta = 0$ when the slender axis of the cylinder is aligned with the separation vector allows for a 1-D spin rate control function $f(\phi)$ to be developed.

Generalization to 3-D Rotations

The torque magnitude presented in Eq. 4 and accompanying orientation angle dependency in Eq. 6 are generalized for 3-D tumbling motion by Eq. 7 and the generic set of three attitude coordinates σ.

$$L = \gamma f(\phi)\, g(\boldsymbol{\sigma}) \tag{7}$$

Because of the axi-symmetric shape of a cylinder and MSM sphere distribution, no torque is generated on the roll rotation about the first body axis $\hat{\boldsymbol{b}}_1$. Returning to the torque produced by the MSM representation in Eq. 3b, the vector $\hat{\boldsymbol{r}}$ between the centers of mass of the two craft is always coplanar with the vectors from servicer sphere to all spheres of the cylinder. Torque is only produced about an axis perpendicular to the defined plane and thus the torque produced is always perpendicular to the vector $\hat{\boldsymbol{r}}$. Therefore the torque axis $\hat{\boldsymbol{e}}_L$ and projection angle Φ about the torque axis are defined as:

$$\hat{\boldsymbol{e}}_L = \hat{\boldsymbol{b}}_1 \times (-\hat{\boldsymbol{r}}) \tag{8}$$

$$\Phi = \cos^{-1}\left(\hat{\boldsymbol{b}}_1 \cdot (-\hat{\boldsymbol{r}})\right) \tag{9}$$

where $\hat{\boldsymbol{r}}$ is the unit separation vector from the servicing spacecraft mass center to the tumbling body mass center. The projection angle and torque axis are shown in Fig. 2. The 3D torque vector is finally expressed as:

$$\hat{\boldsymbol{L}} = L\hat{\boldsymbol{e}}_L \tag{10}$$

The new orientation dependency function $g(\sigma)$ assumes the following form for an axi-symmetric cylinder:

$$g(\boldsymbol{\sigma}) = \sin(2\Phi) \tag{11}$$

The induced charge effect of the MSM spheres dictates that the $g(\sigma)$ function also be dependent on the separation distance. This study primarily considers a long-range

fixed separation distance of $d = 15$m where the induced charging effects are negligible. Assuming a fixed separation distance and electrical potential, Fig. 3a uses the MSM model to illustrate the resulting electrostatic torques on the cylinder where the attitude is parameterized using a 3-2-1 Euler angle sequence through yaw ψ and pitch θ, and a roll rotation angle about $\hat{\boldsymbol{b}}_1$. The torque surfaces are normalized by the largest torque value obtained from all configurations at the set separation distance and potential. Also visible in Fig. 3a is the symmetric character of the torque surface suggesting that the projection angle previously defined sufficiently captures the resulting torque.

Figure 3b illustrates the percent modeling error in torque magnitude if the simplified torque expression in Eq. 7 is used with the newly proposed g-function in Eq. 11. The g-function retains the double-angle sine function form previously studied by Reference [6] for the 1-D case. For example, if the pitch angle were zero, the projection angle would be the rotation angle θ and the control collapses to the 1-D form. Implementation of the projection angle formulation $g(\Phi)$ captures the torque surface in Fig. 3a with a correlation of $R^2 = 0.998$ when separated at $d = 15$ m.

The MSM predicted torque surface is sensitive to separation distance, and the fit quality provided by Eq. 11 decreases rapidly as the separation distance diminishes. The sensitivity to separation distance is shown in Fig. 4 where the MSM predicted torque is shown for a separation distance of $d = 15$ m and $d = 2.5$ m respectively. The change in torque surface character is clearly visible in Fig. 4b where the torques for the cases $d = 15$ m and $d = 2.5$ m are shown respectively.

Comparing the torque surface shapes in Figs. 4a and 4b there are 2 primary differences between the long- and short-range torque profiles. First, with shorter separation distances, the repulsive (negative) torques are significantly smaller in magnitude than the attractive (positive) torques. Second, the surface contour at a given potential level has less resemblance to the earlier double-angle sine function. To capture the variation between short- and long-range torque profile behaviors, a more general orientation dependency function is required.

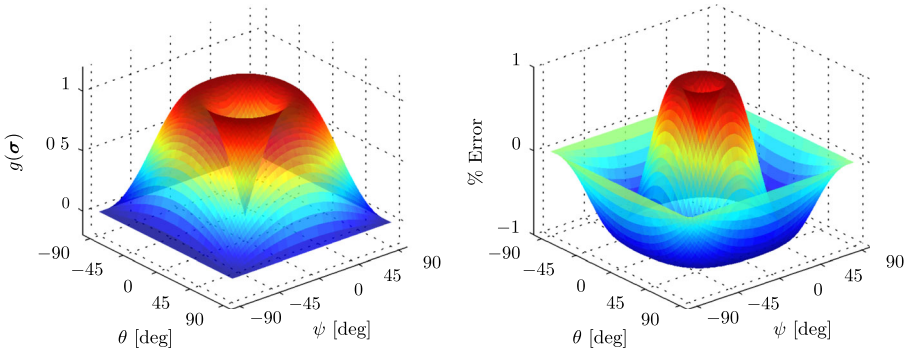

(a) Base function as a function of attitude

(b) Error between base function and MSM

Fig. 3 Normalized torque surface and corresponding error at a separation distance of $d = 15m$ for $V_1 = -30kV$ and $V_2 = 30kV$

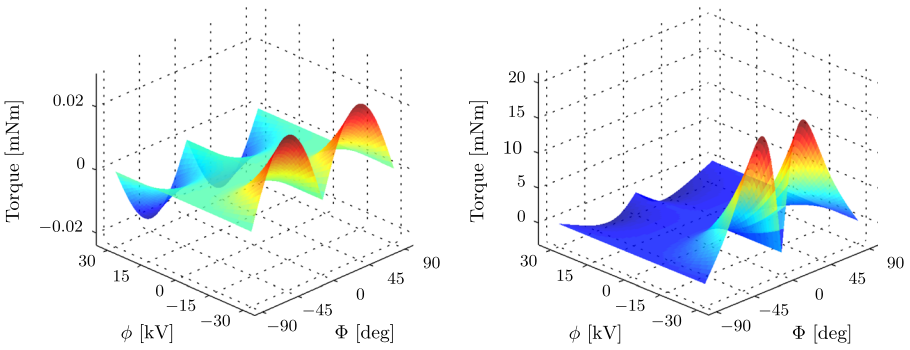

(a) Separation $d = 15$ m (b) Separation $d = 2.5$ m

Fig. 4 MSM torque surfaces at a separation distances of $d = 2.5$ m and $d = 15$ m for $V_1 = -30kV$ and $V_2 = 30kV$

Higher Order Attitude Dependent Torque Scaling Function

The quality of the fit degrades as the separation distance decreases due to the induced charging effects predicted by MSM but not captured by the analytic torque approximation in Eq. 7 and the associated g-function in Eq. 11. The torque approximation is revised to the following series form:

$$L = f(\phi) \sum_{m=1}^{n} \gamma_m g_m(\sigma) \tag{12}$$

where n is the number of terms in the desired approximation and γ_m is the coefficient of the m^{th} term. Inclusion of additional terms in the analytic approximation enables more accurate close proximity fits to the MSM torque representation. Note that while the the torque surface shape profiles vary between short- and long-range evaluations, the sign of the predicted torque is always correct. Having the reduced order torque model retain the correct sign at all times is important when developing spin-stabilizing controls. The series from does provide a closer approximation of charging and therefore detumble performance.

Referring to approximate model errors in Fig. 3b, the error plot resembles the $\sin(4\Phi)$ surface. This motivates the following series approximation:

$$\sum_{m=1}^{n} \gamma_m g_m(\boldsymbol{\sigma}) = \sum_{m=1}^{n} \gamma_m \frac{m!}{d^{2(m-1)}} \sin(2m\Phi) \tag{13}$$

The separation distance appears in the denominator as a "stiffness" like term. Therefore, as the separation distance grows, the higher order terms tend towards zero. This stiffness formulation increases the fit quality across the entire separation distance regime.

Applying the general expansion form to the close proximity profiles in Fig. 4b yields the improved approximation shown in Fig. 5. The profiles shown in Fig. 5 are generated using the expansion in Eq. 13 where all γ_m values are set equal and

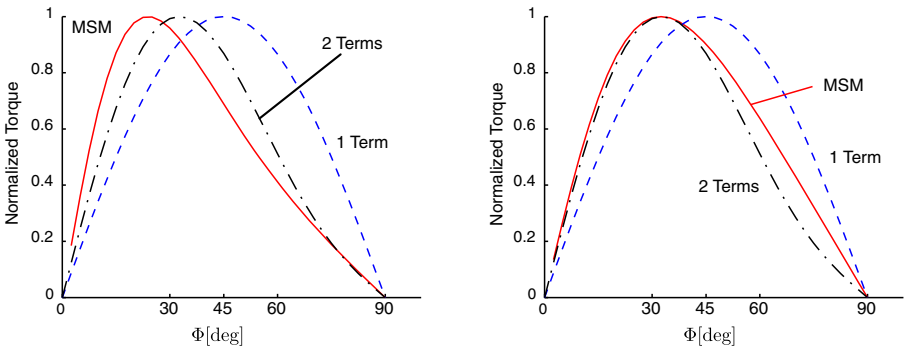

(a) Attractive, $d = 2.5$ m, $f(\phi) < 0$ (b) Repulsive, $d = 2.5$ m, $f(\phi) > 0$

Fig. 5 Additional terms in $g(\Phi)$ approximation of MSM

the torque surface is normalized about the maximum torque value. This removes the search for scaling terms γ_m and more clearly exhibits the surface contour shape fit quality improvement. While improved approximation is gained when implementing higher order terms, only the first order term is considered in the numerical simulations because the separation distance is held fixed at $d = 15$ m. Satellites separated by a distance of $d = 15$ m with the geometry prescribed in this study are outside of substantial induced charge effects where sufficient accuracy is attained through the first order term using $\gamma = 2.234 \times 10^{-14}$ tuned in Reference [6].

Equilibrium States Assuming Constant Potentials

The following developments require that the function $f(\phi)$ in Eq. 12 be invertible and has the property $f(\phi)\phi \geq 0$ enforced by the criteria in Eq. 5 [6]. The three-dimensional rotational equations of motion of a rigid body are given by [26]

$$I\dot{\boldsymbol{\omega}} + \boldsymbol{\omega} \times I\boldsymbol{\omega} = \boldsymbol{L} \tag{14}$$

The equations of motion are rewritten in terms of the projection angle Φ as follows. The principal moments of inertia I_a and I_t represent the axial and transverse components respectively. The coordinate frame $\mathcal{E} : \{\hat{\boldsymbol{b}}_1, \hat{\boldsymbol{e}}_L \times \hat{\boldsymbol{b}}_1, \hat{\boldsymbol{e}}_L\}$ provides a convenient frame in which to express the rotational equations of motion in Eq. 14. The direction cosine matrix $[EB]$ mapping cylinder body-frame $\mathcal{B}$ vector components to $\mathcal{E}$-frame non-body fixed evolving cylinder frame components is

$$[EB] = \begin{bmatrix} 1 & 0 & 0 \\ 0 & -(\hat{\boldsymbol{r}} \cdot \hat{\boldsymbol{b}}_2) & -(\hat{\boldsymbol{r}} \cdot \hat{\boldsymbol{b}}_3) \\ 0 & (\hat{\boldsymbol{r}} \cdot \hat{\boldsymbol{b}}_3) & -(\hat{\boldsymbol{r}} \cdot \hat{\boldsymbol{b}}_2) \end{bmatrix} \tag{15}$$

Recall that $\hat{\boldsymbol{r}}$ is the unit direction from the servicer spacecraft mass center to the tumbling body mass center and the $\hat{\boldsymbol{b}}$ vectors are the body fixed principal frame vectors.

The $\mathcal{E}$-frame is not constant in the body frame as it is dependent on the rotation of the body and the relative position of the two craft. In terms of $\mathcal{E}$-frame components, the angular velocity vector $\boldsymbol{\omega}$ is expressed as:

$$\boldsymbol{\omega} = \omega_1 \hat{\boldsymbol{b}}_1 + \eta(\hat{\boldsymbol{e}}_L \times \hat{\boldsymbol{b}}_1) - \dot{\Phi}\hat{\boldsymbol{e}}_L \tag{16}$$

where η is a angular velocity measure about the current $\hat{\boldsymbol{e}}_L \times \hat{\boldsymbol{b}}_1$ axis. Noting that the moment of inertia about the torque axis $\hat{\boldsymbol{e}}_L$ is always perpendicular to $\hat{\boldsymbol{b}}_1$, Eq. 14 is written in terms of $\mathcal{E}$-frame components to yield the following three scalar differential equations:

$$I_a \dot{\omega}_1 = 0 \tag{17a}$$

$$I_t \dot{\eta} - I_a \omega_1 \dot{\Phi} \sin\Phi = 0 \tag{17b}$$

$$I_t \left(\ddot{\Phi} \sin\Phi - \eta^2 \frac{\cos\Phi}{\sin^2\Phi} \right) + I_a \omega_1 \eta = L \tag{17c}$$

Representing the equations of motion in the projection angle coordinate system $\mathcal{E}$ shows that the control only influences torques around the cylinder's transverse $\hat{\boldsymbol{e}}_L$ axis. Consistent with the assumption of an axi-symmetric geometry, there exists no control authority in the $\hat{\boldsymbol{b}}_1$ axis scalar equation and no cross coupling is present. Thus, ω_1 is constant for all time. In Eq. 17, the angular velocity measures η and $\dot{\Phi}$, as well as the electrostatic control torque $\boldsymbol{L}$, are defined by

$$\eta \equiv -\omega_2(\hat{\boldsymbol{r}} \cdot \hat{\boldsymbol{b}}_2) - \omega_3(\hat{\boldsymbol{r}} \cdot \hat{\boldsymbol{b}}_3) \tag{18a}$$

$$\dot{\Phi} \sin\Phi = -\omega_2(\hat{\boldsymbol{r}} \cdot \hat{\boldsymbol{b}}_3) + \omega_3(\hat{\boldsymbol{r}} \cdot \hat{\boldsymbol{b}}_2) \tag{18b}$$

$$\boldsymbol{L} = -L\hat{\boldsymbol{e}}_L = -f(\phi) \sum_{m=1}^{n} \gamma_m g_m(\Phi)\, \hat{\boldsymbol{e}}_L \tag{18c}$$

The torque free conditions occur at points where the projection angle dependency function is zero or the control voltage Φ becomes zero. These states are present at projection angle orientations $\Phi = \pi n/2$ for $n = 0, 1, 2, 3$ given the form considered in Eq. 13.

Feedback Control Development

The following feedback control development uses rotation rate control to reduce or eliminate the cylinder's tumbling motion. A fixed separation distance is maintained using the inertial thrusting scheme described in Reference [6]. Because it is not possible to generate a general control torque vector, but only a torque about the current $\hat{\boldsymbol{e}}_L$ axis, the 3D detumble control will never achieve asymptotic spin regulation. For example, Eq. 17 shows that if ω_1 is non-zero, the electrostatic torque on this axi-symmetric body will never be able to reduce ω_1 to zero.

The proposed rate controller assumes the projection angle Φ and rate $\dot{\Phi}$ are measured and the commanding spacecraft potential ϕ_1 is the control variable [6]. Revising the control formulation in Reference [6] leads to the new control law $f(\phi_1)$:

$$f(\phi_1) = -\text{sgn}\left(\sum_{m=1}^{n} g_m(\Phi)\right) h(\alpha\dot{\Phi}) \tag{19}$$

where $\alpha > 0$ is a constant feedback gain and the function h is chosen for stability such that[6]:

$$h(x)x > 0 \text{if} x \neq 0 \tag{20}$$

Large tumble rates that tend toward infinity necessitate a limit on commanding a physical potential. The following h function smoothly limits, or saturates, the control at a maximum achievable potential [6].

$$h(\alpha\dot{\Phi}) = f(\phi_{\max})\frac{\arctan(\alpha\dot{\Phi})}{\pi/2} \tag{21}$$

that is

$$\lim_{\dot{\Phi}\to+\infty} f(\phi_1) = \begin{cases} f(\phi_{\max}) & \text{if } \sum_{m=1}^{n} g_m(\Phi) \neq 0 \\ 0 & \text{if } \sum_{m=1}^{n} g_m(\Phi) = 0 \end{cases} \tag{22}$$

This smoothly-saturating performance is compared to the conventional bang-bang controller which always exerts maximum control authority.

$$h(\alpha\dot{\Phi}) = f(\phi_{\max})\text{sgn}(\dot{\Phi}) \tag{23}$$

The saturation controller presented in Eq. 21 becomes the bang-bang controller as α tends to infinity.

Stability Analysis

The stability of the proposed feedback control law in Eq. 19 is explored using the following positive definite candidate Lyapunov function

$$V = \frac{1}{2}\boldsymbol{\omega}^T I \boldsymbol{\omega} \tag{24}$$

The proposed rate control arrests the rotational motion about the transverse cylinder axis and does not seek to arrest the rotational motion about the axi-symmetric body axis nor achieve a specific spacecraft orientation. Taking the time derivative of the candidate Lyapunov function with no torques around the $\hat{\boldsymbol{b}}_1$ axis produces the familiar work-energy form.

$$\dot{V} = \boldsymbol{\omega}^T \boldsymbol{L} = \boldsymbol{\omega}_2 L_2 + \boldsymbol{\omega}_3 L_3 \tag{25}$$

Applying the rotation matrix in Eq. 15 and the equations of motion presented in Eq. 18, the Lyapunov function derivative assumes the form

$$\dot{V} = -L\left(-\dot{\Phi}\sin\Phi\right) = f(\phi_1)\dot{\Phi}\sin\Phi\sum_{m=1}^{n}\gamma_m\sin(2m\Phi) \tag{26}$$

Substituting in the proposed control law presented in Eq. 19 into the Lyapunov derivative in Eq. 26 yields

$$\dot{V} = -\text{sgn}\left(\sum_{m=1}^{n} g_m(\Phi)\right) h(\alpha\dot{\Phi})\dot{\Phi}\sin\Phi \leq 0 \tag{27}$$

This $\dot{V}$ expression is globally negative semi-definite as the orientation dependence summation is positive semi-definite, and the term $h(\alpha\dot{\Phi})\dot{\Phi} \geq 0$, and $\sin(\Phi)$ is positive semi-definite in the range considered. The symmetry of this treatment enables the projection angle to be bounded by $-\pi/2 < \Phi \leq \pi/2$. The bound is justified by the equivalence between a projection angle of $\pi/2 < \Phi \leq \pi$ and a redefined $\hat{\boldsymbol{b}}_1$ to align with the approaching slender axis with $-\pi/2 < \Phi \leq 0$. The restricted range of the projection angle Φ ensures a positive definite value within the control. Furthermore, the largest invariant set where $\dot{V}$ remains zero is $\dot{\Phi} = 0$. Thus, the proposed controller is globally Lyapunov stable and drives the projection angle rate $\dot{\Phi}$ to zero as desired. However, it does not provide any convergence guarantees on the other body rates ω_1 and η, nor does it predict a particular resulting attitude. Insight into the behaviors of Φ, ω_1, and η are gained by further study of Eq. 17.

Steady-State Attitudes and Rates

The Lyapunov result in Eq. 27 guarantees the convergence to a projection angle rate $\dot{\Phi}$ of zero. To remain at this condition, the rotational equations of motion in Eq. 17 are examined further. First, Eq. 17a illustrates that ω_1 will remain constant under the influence of this electrostatic detumble torque. Second, because $\dot{\Phi} \to 0$, Eq. 17b illustrates that the rate measure η will converge to a constant stead-state value η_{ss}. Assuming a steady-state condition has been reached, where $\ddot{\Phi}_{ss} = 0$, allows (17c) to be written as

$$-I_t\eta_{ss}^2\frac{\cos\Phi_{ss}}{\sin^2\Phi_{ss}} + I_a\omega_1\eta_{ss} = 0 \tag{28}$$

which is further simplified assuming η is non-zero:

$$\eta_{ss}\cos\Phi_{ss} = \frac{I_a}{I_t}\omega_1\sin^2\Phi_{ss} \tag{29}$$

Equation 29 provides the final projection angle Φ_{ss} as a function of system parameters and final angular velocities.

The decomposition of torque into the $\mathcal{E}$-frame, used previously by the new equations of motion, can be further applied to study the angular momentum changes with this closed-loop detumble control. Consider the fundamental rotational equations of motion expressed in a non-rotating frame:

$$\dot{\boldsymbol{H}} = \boldsymbol{L} \tag{30}$$

which can be decomposed into vector components perpendicular to and parallel to the invariant unit vector $\hat{\boldsymbol{r}}$ in Eq. 31 with graphical representation in Fig. 6.

$$\boldsymbol{H} = I_a\omega_1\hat{\boldsymbol{b}}_1 + H_{\parallel r}\hat{\boldsymbol{r}} + \boldsymbol{H}_{\perp r} \tag{31}$$

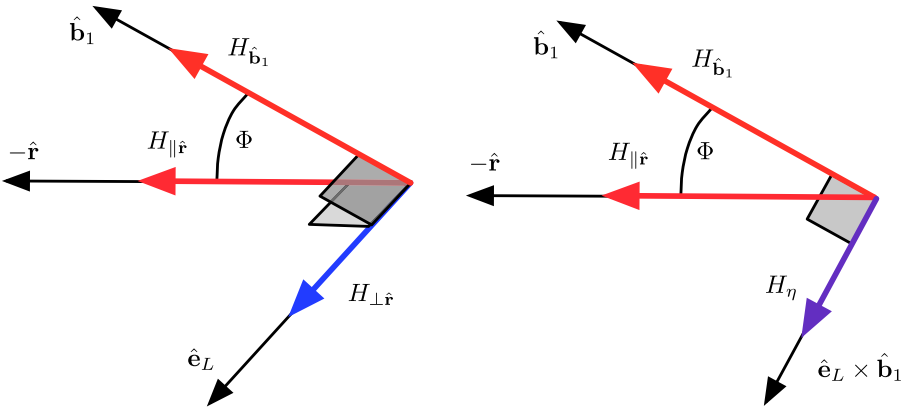

(a) 3D momentum vector components (b) Planar momentum vector components

Fig. 6 Component breakdown of momentum. Colored to represent the ability for detumble influence

In terms of $\mathcal{E}$-frame components, the angular momentum is expressed as

$$\boldsymbol{H} = I_a\omega_1\hat{\boldsymbol{b}}_1 + I_t\eta(\hat{\boldsymbol{e}}_L \times \hat{\boldsymbol{b}}_1) - I_t\dot{\Phi}\hat{\boldsymbol{e}}_L \tag{32}$$

The Lyapunov control analysis presented above demonstrates that the angular momentum component $\boldsymbol{H}_{\perp r}$ is driven to zero. Thus, the steady-state angular momentum vector obtained from Eq. 31 is given by

$$\boldsymbol{H}_{ss} = I_a\omega_1\hat{\boldsymbol{b}}_1 + H_{\parallel r}\hat{\boldsymbol{r}} \tag{33}$$

Because the torque is always perpendicular to $\hat{\boldsymbol{r}}$, the magnitude of the parallel component remains constant through time. Thus, the value can be obtained from the initial momentum of the system.

$$H_{\parallel r} = \left(\boldsymbol{H}(t_0) - I_a\omega_1\hat{\boldsymbol{b}}_1\right)\cdot\hat{\boldsymbol{r}} = \text{constant} \tag{34}$$

Inserting the $\mathcal{E}$-frame components of momentum from Eq. 32 into Eq. 34, the parallel momentum component can be related to the current state via (35).

$$H_{\parallel r} = I_t\eta\sin^2(\Phi) \tag{35}$$

Evaluating (35) with steady state values of η_{ss} and Φ_{ss} while enforcing the equations of motion condition in Eq. 29 predicts the final projection angle, or coning angle, and the angular velocity after the detumble torque history is applied.

The steady-state spin conditions with this touchless detumble control are illustrated through the following 3 cases:

Case 1 Assume both ω_1 and the η are initially zero. In the absence of coupling, the equations of motion enforce $\eta = 0$ for all time. Under these assumptions, the cylinder is undergoing a 1D rotation as discussed in detail in Reference [6]. Equation 29 is satisfied for any angle Φ_{ss}, providing no insight into the final resting attitude. In fact,

for such a 1D rotation scenario, the projection angle at which the cylinder comes to rest is a function of the initial rotation, and thus generally unpredictable.

Case 2 Assume ω_1 is zero and the initial η is non-zero. These assumptions dictate η remains a non-zero constant value for all time due to Eq. 17b. The right hand side of Eq. 29 is zero in this case, requiring that $\cos(\Phi_{ss})$ equal zero. The only resulting attitude given these initial conditions is a projection angle of $\Phi_{ss} = \pm 90°$ with the final η_{ss} determined through (35).

Case 3 Assume ω_1 is non-zero. Regardless of the initial η value, coupling exists and η is in general nonzero. The final η_{ss} and projection angle are determined from Eqs. 35 and 29. The steady state behavior is characterized by a coning motion about the $\hat{\boldsymbol{r}}$ vector with the projection angle, or its supplementary angle, as the cone angle. The final Φ_{ss} angles are illustrated for a range of η_{ss} and ω_1 values, using the parameters from Table 1, in Fig. 7. A special instance of this formulation is where $H_{\|r} = I_a \omega_1$ resulting in a final projection angle of zero.

The control formulation in Eq. 19 is developed assuming both attractive and repulsive electrostatic forces can be implemented. Repulsive forces are always more challenging to implement, leading to the question if the control can be implemented with only attractive forces. As discussed in Reference [6], only using attractive forces doesn't impact the control's stability arguments as $\dot{V}$ remains negative semi-definite in Eq. 27. However, this will have an impact on the control's performance, as the detumble control is only active for approximately half of the time.

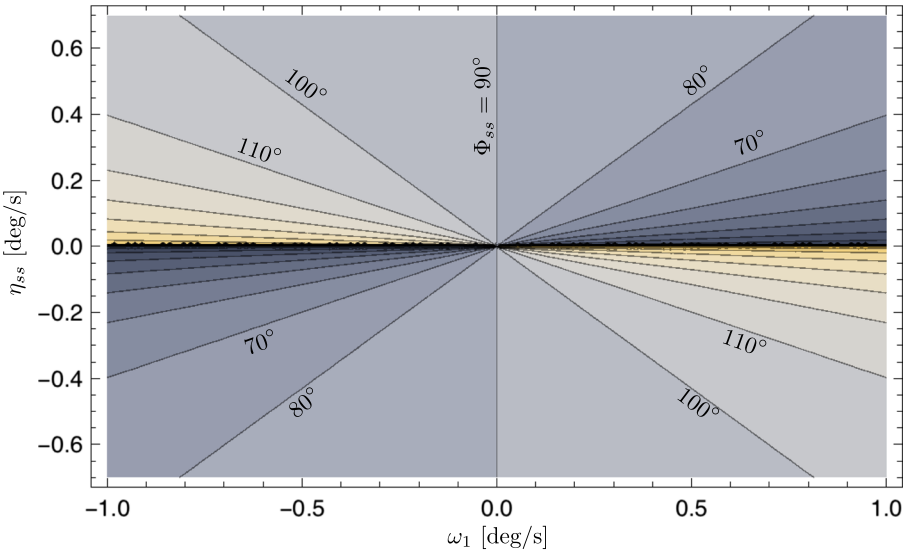

Fig. 7 Correlation between the steady state η, ω_1, and the steady state angle Φ

Numerical Simulation

A numerical simulation is performed to validate the stability and steady-state predictions of the developed control scheme. The simulation places the servicer spacecraft 12.5 meters away from a generally tumbling cylinder in deep space. That is, no perturbations other than the electrostatic interaction are present. The numerical simulation includes the 6-DOF motion of the debris and 3-DOF translational motion of the servicer sphere. A closed-loop servo control is used to maintain a fixed relative position between servicer and debris. A 4^{th} order Runge-Kutta integration is employed with a time step of 0.01 sec. The servicer vehicle potential is controlled via (19), while the electrostatic force is evaluated using the full MSM model in Eqs. 2–3b.

The debris is initially tumbling above $2°/\text{sec}$ with the MSM model parameters presented in Table 1 and the simulation parameters shown in Table 2. Two simulation cases are presented to highlight both the prediction capability and the performance of electrostatic detumble. The first case is in the presence of full coupling through a non-zero ω_1, demonstrating a final coning angle near $\Phi_{ss} = 96.26°$. The second case sets $\omega_1 = 0$ and demonstrates the pure flat spin with a projection angle of $\Phi = 90°$.

Consider the first case where coupling through ω_1 is present. Given the initial conditions of $\omega_0 = [0.5, -1.374, 1.374]$ and $\Phi_0 = 30°$ the proposed controller detumbles the cylinder in less than 260 h. The commanded potential history is shown in Fig. 8a and the projection angle time history is shown in Fig. 8b. Clearly visible in both figures is the reduction of projection angle to the final coning angle of approximately 96.5° whereby the controller commands zero nominal potential. Given the initial conditions the predicted final coning angle $\Phi_{ss} = 96.26°$. The slight deviation from this value is attributed to a true simulation in which the station keeping controller may not keep the commanding craft separated by in the $\hat{\boldsymbol{Y}}$ component. The apparent high frequency in the control, Fig. 8a, and the projection angle, Fig. 8b, is attributed to presenting time in hours. The tumble dynamics with rates less than 10°/sec considered are much slower than the millisecond charging effects. Figure 8c demonstrates that the controller monotonically reduces the rotational kinetic energy

Table 2 Simulation parameters for cylinder detumble system

Parameter	Value	Units	Description
m_C	500	kg	Commanding sphere mass
R_C	2	m	Commanding sphere radius
m_D	1000	kg	Cylinder debris mass
R_D, l_D	1, 3	m	Cylinder radius and length
I_a	125.0	kg·m^2	Cylinder axial moment of inertia
I_t	812.5	kg·m^2	Cylinder transverse moment of inertia
α	5×10^4	–	Gain in h function
ϕ_{max}	20	kV	Max voltage in h function

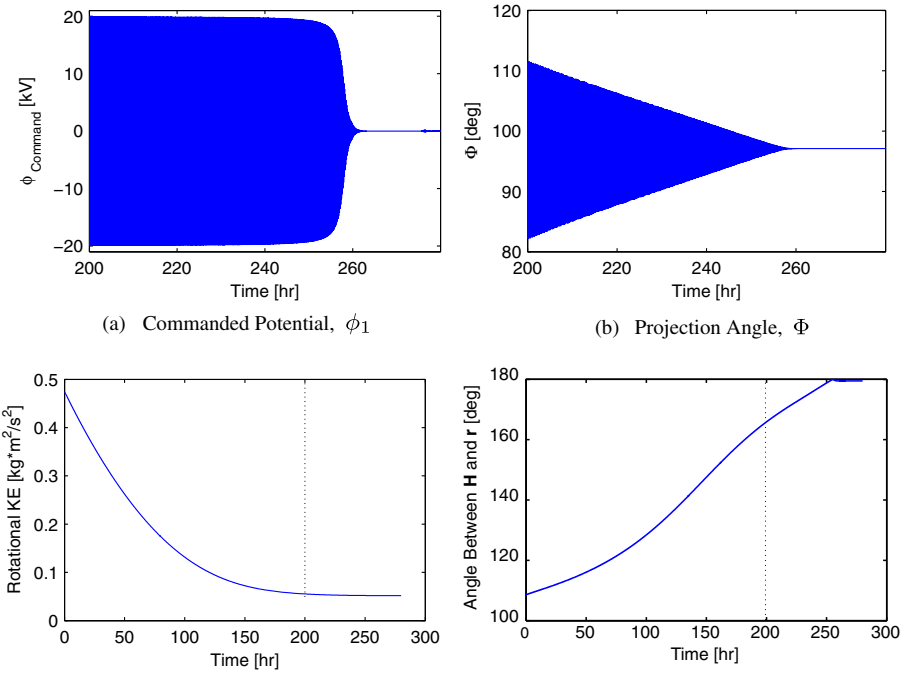

(a) Commanded Potential, ϕ_1 (b) Projection Angle, Φ

(c) Rotational Kinetic Energy (d) Alignment of $\boldsymbol{H}$ and $\boldsymbol{r}$

Fig. 8 Numerical simulation with initial conditions: $\omega = [0.5, -1.374, 1.374]$, $\Phi_0 = 30°$

to the steady state magnitude, $||\boldsymbol{H}_{ss}||$. Furthermore, recalling the momentum arguments such that the remaining momentum vector after detumble must be co-linear with the $\hat{\boldsymbol{r}}$ vector, Fig. 8d shows that the angle between the these two vectors achieve 180°. An angle of either 0 or 180° represents the alignment of $\boldsymbol{H}_{ss}$ and $\hat{\boldsymbol{r}}$.

The reduction of angular velocity and angular momentum is shown in Fig. 9. The body fixed angular velocities, ω_i in Fig. 9a show the reduction to final values

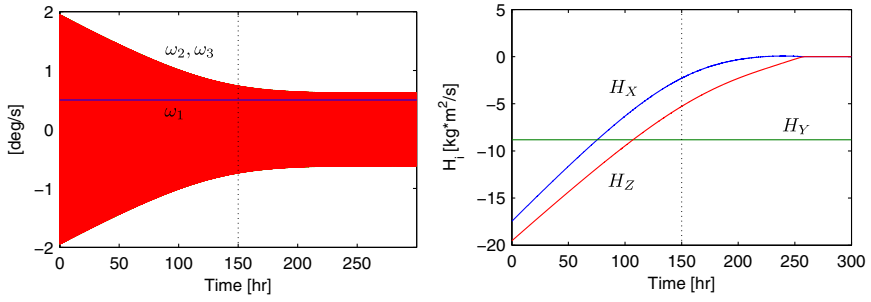

(a) Angular Velocities, ω_i (b) Momentum Components H_i in servicer frame

Fig. 9 Numerical simulation with initial conditions: $\omega = [0.5, -1.374, 1.374]$, $\Phi_0 = 30°$

of ω_2 and ω_3 which exchange magnitudes as the body rotates. This is expected as the non-rotating frame angular momentum along $\hat{\boldsymbol{r}}$ is fixed after detumble requiring the rotating cylinder to have oscillatory body-fixed angular velocity magnitudes. In support of Fig. 8c where the total magnitude is reduced, the non-rotating frame angular momentum components are shown in Fig. 9b. The non-rotating frame component along $\boldsymbol{Y}$ is align with $\hat{\boldsymbol{r}}$ and remains constant where the two perpendicular components H_x and H_z are driven to zero.

The $\Phi - \dot{\Phi} - \eta$ phase space of the case presented provides further insight into the behavior of η over time. Figure 10a shows the first 5000 sec following detumble activation. The peaks visible characterize the minimum magnitude of η possible which corresponds to the final η magnitude. The convergence on the final Φ is shown in Fig. 10b where the phase space has flattened to the minimum magnitude η. This value of eta is predicted by the momentum arguments of Eq. 35. The phase space view further demonstrates the predictability of the final resting attitude using momentum based arguments.

The same initial conditions shown in the first case, Fig. 8, are used to initialize the second case in Figure 11 although the coupling term ω_1 has been set to zero. Figure 11b shows the uncoupled steady state projection angle to be $\Phi_{ss} = 90°$ as Eq. 29 predicts. Without the coupling, the commanded potential remains large over the longer time window shown in Fig. 11a. Consistent with prediction and the first simulation case, the angular momentum magnitude is reduced to the steady state value. Also clear is the co-linear alignment of angular momentum with the $\hat{\boldsymbol{r}}$ shown in Fig. 11d.

The absence of coupling reduces the effectiveness of the detumble controller. The component magnitudes of body-fixed angular velocity and non-rotating frame angular momentum magnitudes are shown for the uncoupled case in Fig. 12. The oscillatory exchange of angular velocity is no longer present due to the absence of coupling, although the magnitude of the non-oscillating case matches the peak values shown for the first case in Fig. 9a. The component angular momentum reduction for the second case retains the constant H_y magnitude and drives the perpendicular components to zero, however the time scale is much longer than the coupled case.

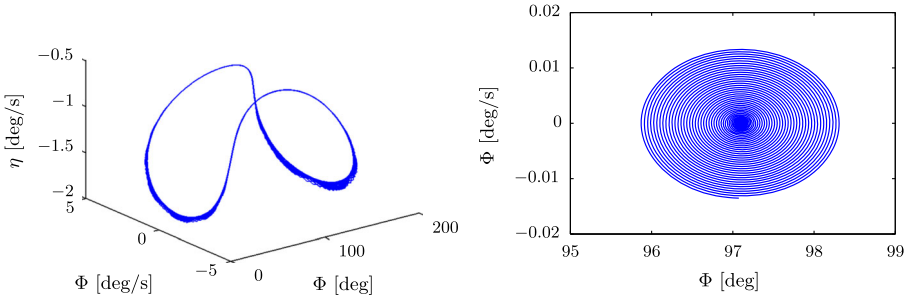

(a) Initial 5000 Seconds (b) Final 27 Hours

Fig. 10 Phase Space with initial conditions: $\omega = [0.5, -1.374, 1.374]$, $\Phi_0 = 30°$ displayed at 5 second intervals

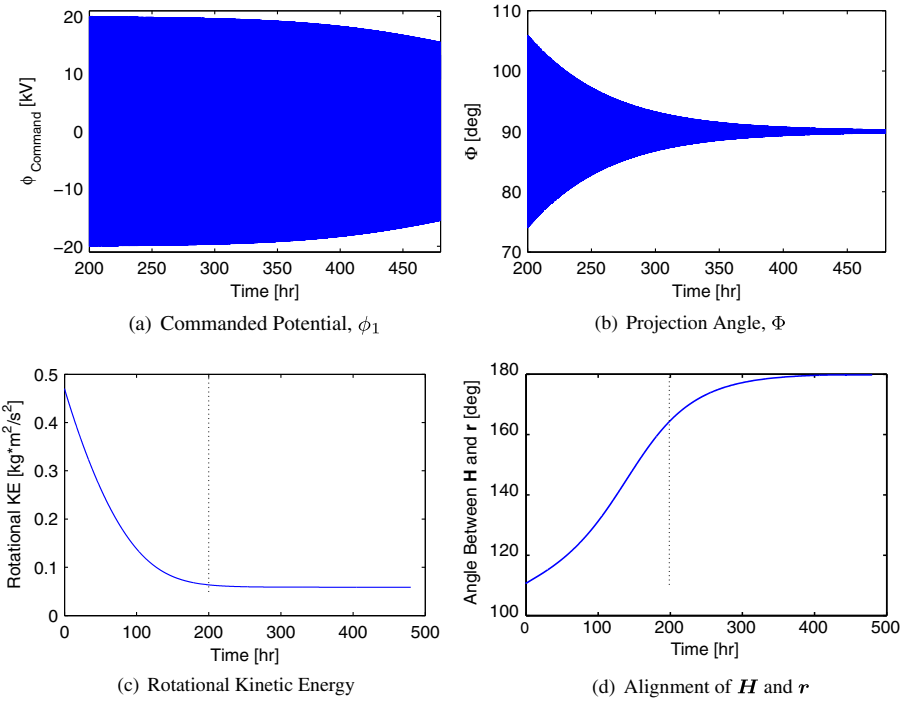

(a) Commanded Potential, ϕ_1 (b) Projection Angle, Φ

(c) Rotational Kinetic Energy (d) Alignment of $\boldsymbol{H}$ and $\boldsymbol{r}$

Fig. 11 Numerical simulation with initial conditions: $\omega = [0.0, -1.374, 1.374]$, $\Phi_0 = 30°$

Without coupling, the control requires a substantially more time to reduce the system motion to the previously obtained level. Comparison of Figs. 8 and 11 reveals that the uncoupled case requires twice as long to reach steady state values. Furthermore, since the angular momentum along the separation vector, $H_{\|r}$, is equivalent in both cases then the momentum removed is equivalent. The presented cases suggest that coupling contributes to a more sustained control influence with the opportunity to remove additional angular momentum with a more rapid settling time.

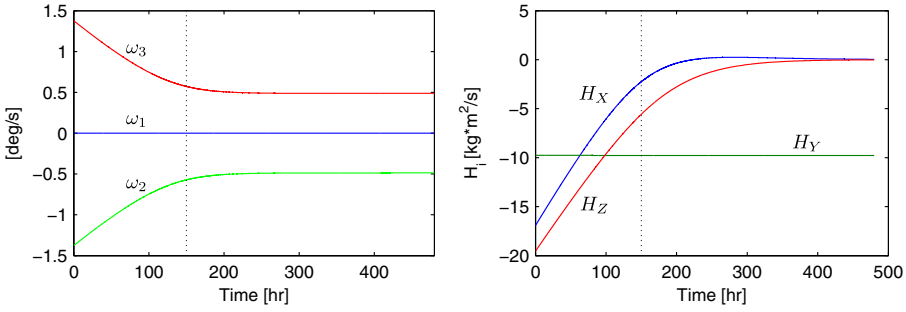

(a) Angular Velocities, ω_i (b) Momentum Components H_i

Fig. 12 Numerical simulation with initial conditions: $\omega = [0.0, -1.374, 1.374]$, $\Phi_0 = 30°$

The control formulation presented provides comparable performance to the bang-bang controller. As seen in both Figs. 8a and 11a the proposed controller is primarily saturated. Thus the bang-bang controller does not provide significant performance gains until most of the momentum has be reduced. The smoothed controller proposed is recommended as it removes the chatter at small projection angle rates otherwise experienced by a bang-bang controller.

Conclusions

The rate-based electrostatic attitude control is investigated for the three-dimensional tumbling motion of a representative cylindrical body. The electrostatic control authority at separation distances on the order of 3 to 4 craft radii demonstrates that the tumbling rotational motion is greatly reduced. More rapid detumble is possible with reduced separation distance and the presence of coupled dynamics for the tumbling body. The control scheme utilizes a general approximation of the multi-sphere modeling method to verify closed-loop stability. The general approximation generalizes previous work and enables stability analysis for close-proximity distances. The control scheme is analytically proven to arrest the tumbling motion and settle in a stable torque equilibrium orientation. The numerical simulation also highlights the movement towards specific orientations dependent on initial conditions. Future work will analyze three-dimensional nominal tugging or pushing, control coast segments, and investigate the torques on more complex geometries.

References

1. Karavaev, Y.S., Kopyatkevich, R.M., Mishina, M.N., Mishin, G.S., Papushev, P.G., Shaburov, P.N.: The dynamic properties of rotation and optical characteristics of space debris at geostationary orbit. Adv. Astronaut. Sci. **119**, 1457–1466 (2004). Paper No. AAS-04-192
2. Couzin, P., Teti, F., Rembala, R.: Active Removal of Large Debris : Rendez-vous and Robotic Capture Issues. 2nd European Workshop on Active Debris Removal, Paris, France (2012). Paper #7.5
3. Couzin, P., Teti, F., Rembala, R.: Active Removal of Large Debris: System approach of deorbiting concepts and Technological issues. In: 6th European Conference on Space Debris, Darmstadt, Germany, April 22–25 2013. Paper No. 6a.P-17
4. Ogilvie, A., Allport, J., Hannah, M., Lymer, J.: Autonomous satellite servicing using the orbital express demonstration manipulator system. In: Proceedings of the 9th International Symposium on Artificial Intelligence, Robotics and Automation in Space (i-SAIRAS'08), pp. 25–29 (2008)
5. Xu, W., Liang, B., Li, B., Xu, Y.: A universal on-orbit servicing system used in the geostationary orbit. Adv. Space Res. **48**(1), 95–119 (2011). doi:10.1016/j.asr.2011.02.012
6. Schaub, H., Stevenson, D.: Prospects Of Relative Attitude Control Using Coulomb Actuation. In: Jer-Nan Juang Astrodynamics Symposium, College Station, TX, June 25–26 2012. Paper AAS 12–607
7. Schaub, H., Moorer, D.F.: Geosynchronous Large Debris Reorbiter: Challenges and Prospects. In: AAS Kyle T. Alfriend Astrodynamics Symposium, Monterey, CA, May 17–19 2010. Paper No. AAS 10-311
8. Moorer, D.F., Schaub, H.: Hybrid Electrostatic Space Tug. US Patent 0036951-A1, 17 (2011)
9. Moorer, D.F., Schaub, H.: Electrostatic Spacecraft Reorbiter. US Patent 8,205,838 B2, 17 (2011)
10. Murdoch, N., Izzo, D., Bombardelli, C., Carnelli, I., Hilgers, A., Rodgers, D.: Electrostatic tractor for near Earth object deflection. 59th International Astronautical Congress, Glasgow Scotland (2008). Paper IAC-08-A3.I.5

11. Murdoch, N., Izzo, D., Bombardelli, C., Carnelli, I., Hilgers, A., Rodgers, D.: The Electrostatic Tractor for Asteroid Deflection (2008). Paper IAC-08-A3.I.5
12. Cover, J.H., Knauer, W., Maurer, H.A.: Lightweight Reflecting Structures Utilizing Electrostatic Inflation. US Patent 3,546,706 (1966)
13. King, L.B., Parker, G.G., Deshmukh, S., Chong, J.-H.: Spacecraft Formation-Flying using Inter-Vehicle Coulomb Forces. Technical Report, NASA/NIAC (2002). http://www.niac.usra.edu
14. Berryman, J., Schaub, H.: Analytical charge analysis for 2- and 3-craft coulomb formations. AIAA J. Guid. Control Dyn. **30**, 1701–1710 (2007)
15. Seubert, C.R., Panosian, S., Schaub, H.: Analysis of a tethered coulomb structure applied to close proximity situational awareness. ASIA J. Spacecr. Rocket. **49**, 1183–1193 (2012)
16. Stiles, L.A., Schaub, H., Maute, K.K., Moorer, D.F.: Electrostatically inflated gossamer space structure voltage requirements due to orbital perturbations. Acta Astronaut. **84**, 109–121 (2013). doi:10.1016/j.actaastro.2012.11.007
17. Wang, S., Schaub, H.: Nonlinear charge control for a collinear fixed shape three-craft equilibrium. AIAA J. Guid. Control Dyn. **34**, 359–366 (2011). doi:10.2514/1.52117
18. Peck, M.A.: Prospects and Challenges for Lorentz-Augmented Orbits. In: AIAA Guidance, Navigation and Control Conference, San Francisco, CA, August 15–18 2005. Paper No. AIAA 2005-5995
19. Streetman, B., Peck, M.A.: New synchronous orbits using the geomagentic lorentz force. AIAA J. Guid. Control. Dyn. **30**, 1677–1690 (2007)
20. Stiles, L.A., Schaub, H., Maute, K., Moorer, D.F.: Electrostatic Inflation of Membrane Space Structures. In: AAS/AIAA Astrodynamics Specialist Conference, Toronto, Canada, Aug. 2–5 2010. AIAA-2010-8134
21. Stevenson, D., Schaub, H.: Multi-sphere method for modeling electrostatic forces and torques. Adv. Space Res. **51**, 10–20 (2013). doi:10.1016/j.asr.2012.08.014
22. Stevenson, D.: Optimization of Sphere Population for Electrostatic Multi Sphere Model. In: 12th Spacecraft Charging Technology Conference, Kitakyushu, Japan, May 14–18 (2012)
23. Stevenson, D., Schaub, H.: Terrestrial Testbed For Remote Coulomb Spacecraft Rotation Control. International Journal of Space Science and Engineering **2**(1), 96–112 (2014). doi:10.1504/IJSPACESE.2014.060111
24. Smythe, W.R.: Static and Dynamic Electricity, 3rd. McGraw–Hill (1968)
25. Sliško, J., Brito-Orta, R.A.: On approximate formulas for the electrostatic force between two conducting spheres," Am. J. Phys. **66**(4), 352–355 (1998)
26. Schaub, H., Junkins, J.L.: Analytical Mechanics of Space Systems, 2nd. Reston, VA: AIAA Education Series (2009)